

**Gregory M. Fomovsky and Jeffrey W. Holmes**

*Am J Physiol Heart Circ Physiol* 298:221-228, 2010. First published Nov 6, 2009;  
doi:10.1152/ajpheart.00495.2009

**You might find this additional information useful...**

---

This article cites 22 articles, 13 of which you can access free at:

<http://ajpheart.physiology.org/cgi/content/full/298/1/H221#BIBL>

Updated information and services including high-resolution figures, can be found at:

<http://ajpheart.physiology.org/cgi/content/full/298/1/H221>

Additional material and information about *AJP - Heart and Circulatory Physiology* can be found at:

<http://www.the-aps.org/publications/ajpheart>

---

This information is current as of August 11, 2010 .

# Evolution of scar structure, mechanics, and ventricular function after myocardial infarction in the rat

Gregory M. Fomovsky<sup>1</sup> and Jeffrey W. Holmes<sup>2</sup>

<sup>1</sup>Department of Biomedical Engineering, Columbia University, New York, New York; and <sup>2</sup>Departments of Biomedical Engineering and Medicine, Robert M. Berne Cardiovascular Research Center, University of Virginia, Charlottesville, Virginia

Submitted 1 June 2009; accepted in final form 3 November 2009

**Fomovsky GM, Holmes JW.** Evolution of scar structure, mechanics, and ventricular function after myocardial infarction in the rat. *Am J Physiol Heart Circ Physiol* 298: H221–H228, 2010. First published November 6, 2009; doi:10.1152/ajpheart.00495.2009.—The mechanical properties of the healing scar are an important determinant of heart function following myocardial infarction. Yet the relationship between scar structure, scar mechanics, and ventricular function remains poorly understood, in part because no published study has tracked all of these factors simultaneously in any animal model. We therefore studied the temporal evolution of scar structure, scar mechanics, and left ventricular (LV) function in large anterior myocardial infarcts in rats. At 1, 2, 3, and 6 wk after left anterior descending coronary ligation, we examined LV function using sonomicrometry, infarct mechanical properties using biaxial mechanical testing, infarct structure using polarized light microscopy, and scar collagen content and cross-linking using biochemical assays. Healing infarcts in the rat were structurally and mechanically isotropic at all time points. Collagen content increased with time and was the primary determinant of scar mechanical properties. The presence of healing infarcts influenced systolic LV function through a rightward shift of the end-systolic pressure-volume relationship (ESPVR) that depended on infarct size, infarct collagen content, and LV dilation. We conclude that in sharp contrast to previous reports in large animal models, healing infarcts are structurally and mechanically isotropic in the standard rat model of myocardial infarction. On the basis of the regional strain patterns we observed in healing rat infarcts in this study and in healing pig infarcts in previous studies, we hypothesize that the local pattern of stretching determines collagen alignment in healing myocardial infarct scars.

collagen; heart; pressure-volume relationship; biaxial mechanics; anisotropy

HEART MUSCLE LOST during a myocardial infarction (heart attack) is gradually replaced by scar tissue. The mechanical properties of the healing scar are an important determinant of heart function. Yet the relationship among scar structure, scar mechanics, and ventricular function remains poorly understood, in part because no published study has tracked all of these factors simultaneously in any animal model (8).

Studies of infarct mechanics suggest that collagen content alone cannot explain the mechanical properties of healing myocardial scar. In sheep, the mechanical properties of healing scar reportedly decoupled from collagen content after the first 2 wk (6). In pigs, strong alignment of collagen fibers created structural and mechanical anisotropy in healing scar tissue (10). In rabbits, cross-linking was an important determinant of the mechanical properties of healing infarcts (3). Unfortunately, none of these studies analyzed left ventricular (LV)

function during infarct healing. Instead, functional studies have focused on rats, where large infarcts that significantly alter LV function are more easily created (18).

We therefore studied the temporal evolution of scar structure, scar mechanics, and LV function in the standard rat infarct model. Our goal was to establish a baseline for subsequent studies in which we planned to modify infarct anisotropy and measure resulting changes in LV function. To our surprise, healing infarcts in the rat were structurally and mechanically isotropic, and collagen content, rather than fiber alignment or cross-linking, was the primary determinant of mechanical properties.

## METHODS

All studies were performed in accordance with the Guide for the Care and Use of Laboratory Animals and approved by our Institutional Animal Care and Use Committee. We created large, transmural anteroapical infarcts in rats by permanent ligation of the left anterior descending coronary artery (4). Animals were anesthetized with an intraperitoneal injection of ketamine (80 mg/kg) and xylazine (5 mg/kg), intubated, and ventilated with room air. A left thoracotomy was performed and the left anterior descending coronary artery was permanently occluded with a 7-0 suture. The chest was closed in layers. Subcutaneous buprenorphine (0.05 mg/kg) was administered immediately, with additional doses every 12 h as required for postoperative pain.

A total of 111 Sprague-Dawley adult male rats were used for these studies. Ninety-nine animals ( $297 \pm 29$  g, Taconic Farms, Germantown, NY) underwent the ligation procedure described above, with an initial mortality of 35%. The 64 surviving animals were euthanized at 1, 2, 3, or 6 wk after ligation: 26 underwent functional studies followed by mechanical testing and histological analysis of the infarct scar ( $n = 7$  at 1 wk, 5 at 2 wk, 8 at 3 wk, 6 at 6 wk), 14 provided scars for biochemical analysis ( $n = 4$  at 1 wk, 3 at 2 wk, 3 at 3 wk, 4 at 6 wk), and 24 were excluded because the infarcts were nontransmural or too small for mechanical testing. To provide a baseline for functional and regional deformation data, we performed acute functional studies as described below on 12 additional rats, successfully acquiring data before and 15 min after coronary ligation in 6.

**Functional studies.** Animals were anesthetized with isoflurane in 100% O<sub>2</sub> (5.0% induction, 2.5% maintenance), intubated via tracheotomy, and ventilated with positive-pressure ventilation. The chest was opened via midline sternotomy with careful attention to hemostasis. Seven sonomicrometer crystals (Sonometrics, London, Ontario, Canada) were sewn to the epicardial surface of the left ventricle (LV): a base-apex (BA) pair for long-axis measurement, an anterior-posterior (AP) equatorial pair for short-axis measurement, and three additional crystals for local strain measurement in the infarct region. A Millar SP-671 pressure transducer (Millar Instruments, Houston, Texas) was inserted into the LV cavity through the anterior wall. Data were acquired at 312 Hz by using the commercial software SonoLab (Sonometrics). After an initial baseline recording, hemodynamic measurements were taken at a range of preload and afterload pressures during temporary occlusions of the inferior vena cava (IVC) and aorta

Address for reprint requests and other correspondence: J. Holmes, Box 800759, Health System, Charlottesville, VA 22908 (e-mail: holmes@virginia.edu).

(Ao). The heart was arrested by retrograde perfusion with cold 2,3-butanedione monoxime (BDM, Sigma Biochemicals, St. Louis, MO) in phosphate-buffered saline (PBS) and removed. In the acute ischemia group, appropriate placement of crystals in the infarct region was confirmed by perfusion with 2% Evans blue (Sigma) in PBS; no histology or mechanical testing was performed. In all other groups, a rectangular sample of the infarct scar (10–15 mm on each side) with edges aligned along the in vivo circumferential and longitudinal directions was dissected for mechanical testing and histology.

Functional data were analyzed via a series of custom algorithms written in MATLAB (v7.0, The MathWorks, Natick, MA). The volume enclosed by the epicardial surface was computed from BA and AP segment lengths assuming a truncated ellipsoidal geometry for the LV (7). Wall volume was computed from measured postmortem mass assuming a density of 1.06 g/cm<sup>3</sup> and subtracted from epicardial volume to obtain cavity volume (V):

$$V = 1.125(\pi/6)AP^2BA - WV \tag{1}$$

The ratio of short-axis to long-axis epicardial radii was computed as (1/2)×AP/(2/3)×BA (7). For each cardiac cycle, end-diastolic (ED) points were selected immediately before the sharp increase in LV pressure, end-systolic (ES) points at maximum elastance (ratio of LV pressure to LV volume), as previously described (7). Points from baseline, IVC occlusion, and Ao occlusion cycles were combined to form end-diastolic (EDPVR) and end-systolic (ESPVR) pressure-volume relationships reflecting global heart function. End-diastolic volume at 10 cmH<sub>2</sub>O pressure (V<sub>10</sub>) was taken as an index of global chamber dilation. The slope and intercept of the linear region of the ESPVR were employed as indexes of systolic function. Average cardiac output (CO) and ejection fraction (EF) for baseline cycles were also computed from heart rate (HR), end-diastolic (EDV), and end-systolic (ESV) volumes as CO = HR × (EDV – ESV) and EF = (100%) (EDV – ESV)/EDV.

**Mechanical testing.** We conducted planar biaxial testing of infarct scars using a device similar to the one described previously by Sacks and Chuong (19). Each sample was submerged in a cold BDM solution and mounted with its circumferential (X<sub>1</sub>) and longitudinal (X<sub>2</sub>) axes aligned with the loading axes. Two small hooks per side were used to grip the sample, and markers were used for optical

tracking of in-plane deformation at the center of the sample. Finite-element simulations of a typical point-loaded sample confirmed that strains were homogenous in the central region where our markers were placed and revealed that the distance between attachment points provided a good estimate of effective side length for stress calculations. A series of load control test protocols with load ratios chosen to cover the X<sub>1</sub>:X<sub>2</sub> stretch plane (Fig. 1A) were performed from a 1-g preloaded state. Each test consisted of 10 cycles at stretch rates ≤2%/s, with the loading portion of the final cycle used for analysis.

Scar samples were small (10–15 mm per side) but thin (1–2 mm), so plane stress was assumed. Surface area and effective side lengths were digitized from images captured at the reference 1-g preloaded configuration preceding the 10th cycle of each test run. The average thickness of the sample was estimated from its measured mass and surface area assuming a tissue density of 1.06 g/cm<sup>3</sup>. Undeformed cross-sectional areas normal to the X<sub>1</sub> (A<sub>1</sub>) and X<sub>2</sub> (A<sub>2</sub>) axes were computed as effective side lengths (distance between attachment points) multiplied by average sample thickness. Components of the deformation tensor **F** were computed from recorded marker coordinates every 100 ms during each test run. Cauchy stresses at each time point were found from measured forces and undeformed areas as

$$t_{11} = \frac{f_1}{A_1} \sqrt{\lambda_1^2 + \kappa_1^2}, \quad t_{22} = \frac{f_2}{A_2} \sqrt{\lambda_2^2 + \kappa_2^2}, \tag{2}$$

$$t_{12} = t_{21} = t_{13} = t_{31} = t_{32} = t_{23} = t_{33} = 0,$$

where f<sub>1</sub>, t<sub>11</sub> and f<sub>2</sub>, t<sub>22</sub> are measured forces and normal Cauchy stresses in the circumferential and longitudinal directions, respectively, and λ and κ are components of the deformation gradient tensor **F**. Unlike prior planar biaxial tests of soft tissues (19, 23), we did not know fiber orientations in our samples prior to testing and therefore could not align the predominant fiber direction with a test axis. Equation 2 therefore reflects the fact that in our device the applied loads remained aligned with the test axes but the sample was free to shear (see APPENDIX for derivation).

For a solid, hyperelastic, nonlinear, homogeneous, incompressible material under quasi-static isothermal conditions, the general constitutive relationship between stress and deformation is

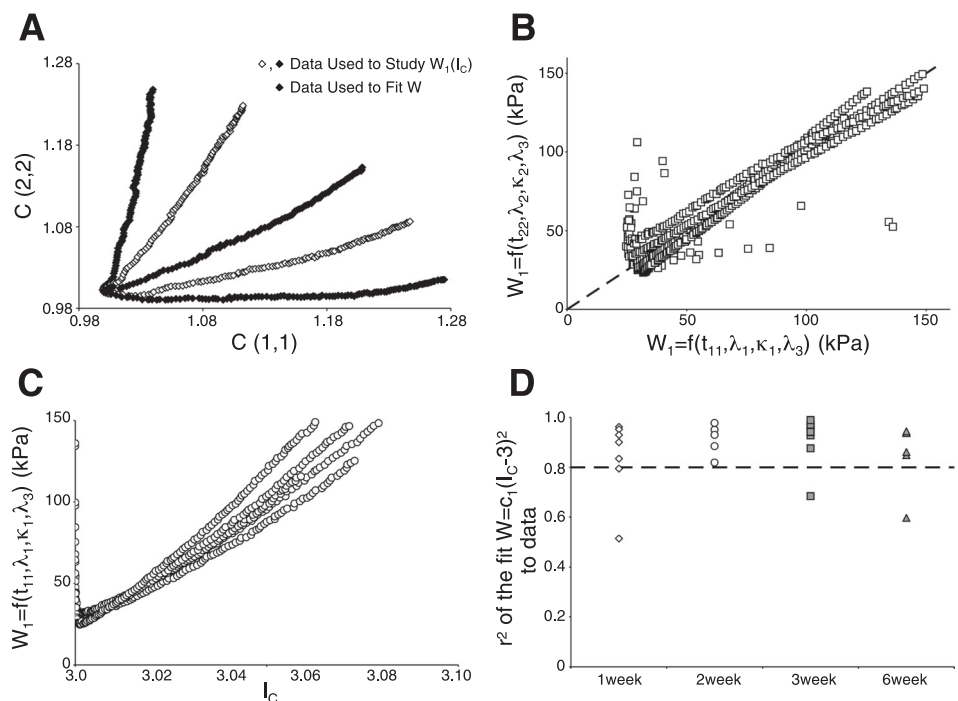


Fig. 1. Illustration of the procedure for choosing the form of the strain energy function, using data from a representative sample (MI170, 3-wk group). A: multiple biaxial test runs provided data across the stretch plane. B: estimates of the response function  $W_1$  from 2 different stress components,  $W_1 = f(t_{11}, \lambda_1, \kappa_1, \lambda_3)$  and  $W_1 = f(t_{22}, \lambda_2, \kappa_2, \lambda_3)$ , agreed well, suggesting that both stresses depended primarily on  $W_1$  and strain energy could be treated as a function of the first invariant  $I_C$ . C: a linear relationship between the response function  $W_1$  and the first invariant  $I_C$  suggested the quadratic form  $W = c_1(I_C - 3)^2$  for the strain energy function. D: the chosen strain energy function fit the majority of samples well ( $r^2 > 0.80$ ). See main text for definitions.

$$\mathbf{t} = -p\mathbf{I} + 2\mathbf{F} \cdot \frac{\partial W}{\partial \mathbf{C}} \cdot \mathbf{F}^T, \quad (3)$$

where  $W$  is a strain energy function and  $\mathbf{C}$  is the right Cauchy-Green deformation tensor. Following Humphrey et al. (12), we assumed that  $W$  depends on the invariants of  $\mathbf{C}$  and used biaxial test data to guide the choice of a polynomial form. In general, for a transversely isotropic material  $W$  can be a function of the first five invariants of  $\mathbf{C}$ :  $W(I_C, II_C, III_C, IV_C, V_C)$ . Because our structural analysis suggested little anisotropy, however, we began by testing how well a function of the first invariant,  $W(I_C)$ , could describe our mechanical data. If  $W$  depends only on  $I_C$ , then the stress components  $t_{11}$  and  $t_{22}$  depend only on the response function  $W_1 = dW/dI_C$  and measured components of the deformation gradient tensor  $\mathbf{F}$ . We therefore compared estimates of  $W_1$  derived from  $t_{11}$ ,  $\lambda_1$ , and  $\kappa_1$  with estimates derived from  $t_{22}$ ,  $\lambda_2$ , and  $\kappa_2$ :

$$W_1 = \left(\frac{1}{2}\right) \frac{t_{11}}{\lambda_1^2 + \kappa_1^2 - \lambda_3^2}, \quad W_1 = \left(\frac{1}{2}\right) \frac{t_{22}}{\lambda_2^2 + \kappa_2^2 - \lambda_3^2}. \quad (4)$$

We found that  $W_1$  computed in these two ways agreed very well (Fig. 1B), suggesting that a function of the first invariant was sufficient to describe the response of the infarcts we tested. Plots of the response function  $W_1$  against  $I_C$  were linear (Fig. 1C), suggesting a quadratic form for  $W(I_C)$ :

$$W = c_1(I_C - 3)^2. \quad (5)$$

We chose three test runs for each sample: one close to equibiaxial stretch, and two close to the outer edges of the stretch plane (Fig. 1A). We represented each run with 50  $t_{11}$  and  $t_{22}$  values spaced equally along the stress axis. The best-fit value of  $c_1$  was determined as the least-squares solution to the overdetermined system of equations:

$$\begin{aligned} t_{11} &= 4c_1(I_C - 3)(\lambda_1^2 + \kappa_1^2 - \lambda_3^2), \\ t_{22} &= 4c_1(I_C - 3)(\lambda_2^2 + \kappa_2^2 - \lambda_3^2). \end{aligned} \quad (6)$$

**Structural and biochemical analysis.** Following mechanical testing, infarct scars were weighed and fixed overnight in formalin. Tissue samples were processed by serial dehydration, clearing, and paraffin embedding, then sectioned parallel to the epicardial surface at 7- $\mu$ m thickness. Ten slides were chosen at evenly spaced transmural depths, stained with picosirius red, and imaged. Infarct area was estimated by averaging manually digitized infarct areas from images of the 10 sections obtained with a Canon PowerShot digital camera.

Analysis of collagen content and orientation focused on the central region of the sample, where the deformation was tracked during biaxial testing. We adopted the method for quantitative structural analysis developed by Whittaker et al. (22), which relies on the fact that fibrillar collagen is the only component in a tissue section stained with picosirius red that is both birefringent (bright under polarized light) and highly acidophilic (dark red under bright-field). Images were acquired with a  $\times 10$  objective lens on an Olympus BX51 polarizing microscope, modified for observation with circularly polarized light (5), by use of a Sony XCD-X710 digital microscope camera (8 bit, monochrome,  $1,024 \times 768$  pixels, 1/3-in. charge-coupled device chip). The field of view at  $\times 10$  magnification was  $0.48 \times 0.36$  mm. A  $1.5 \times 1.5$  mm grid was applied to the coverslip of each slide at the same orientation relative to the sample. The same 10 fields in the central region of the sample were imaged at each transmural depth.

For each field, a bright-field image was digitally subtracted from a polarized image to isolate collagen fibers. Thresholding of this subtraction image was used to identify collagen pixels, and thresholding of the bright-field image was used to identify tissue pixels. Collagen content was computed as the ratio of collagen to tissue pixels. Collagen fiber orientation was measured in the subtraction image by using custom-written MATLAB software MatFiber, an adaptation of

Fiber3, originally developed by Karlon et al. (13) at University of California San Diego. MatFiber software uses an intensity-gradient-detection algorithm to measure orientation (angle measurements between  $-90$  and  $+90^\circ$ ) of the structures in finite subregions of the image ( $40 \times 40$ -pixel subregions were used). The resulting angular histograms showed the fraction of collagen fibers oriented within each  $5^\circ$  arc, and the sum of all fractions was 1.0. Prior to averaging, histograms were scaled by collagen area fraction so that areas containing more collagen contributed more to the average. Histograms were averaged across 10 fields for each section, then 10 transmural depths to obtain one histogram representing collagen alignment for each infarct. These infarct histograms were weighted equally when computing the average histogram for each group (1 wk, 2 wk, etc.), but the group histograms were again scaled by mean area fraction for display, so that increased collagen content is apparent as increased area under the histogram.

A separate group of 14 rats was used in collagen hydroxyproline (OH-pro) and hydroxylsypyrindoline (HP) assays. On the study day, no functional or mechanical studies were performed. Instead, hearts were arrested by retrograde perfusion with cold BDM and excised. Infarct scars were dissected, immediately frozen, and stored at  $-80^\circ\text{C}$ . Biochemical assays for OH-pro and HP were performed as described by McCormick et al. (15). Tissue samples were lyophilized, weighed, hydrolyzed (6 N HCl,  $110^\circ\text{C}$  for 24 h), dried, and resuspended in 1.5 ml of acetic acid. Triplets from each sample were analyzed:  $3 \times 100 \mu\text{l}$  aliquots were used in OH-pro and  $3 \times 400 \mu\text{l}$  in HP assays. OH-pro concentration was determined by the colorimetric technique with isodesmosine as a standard. The results (average of the triplets) were reported as %collagen based on the dry weight of each sample and the assumption that the weight of collagen is 7.42 times that of OH-pro.

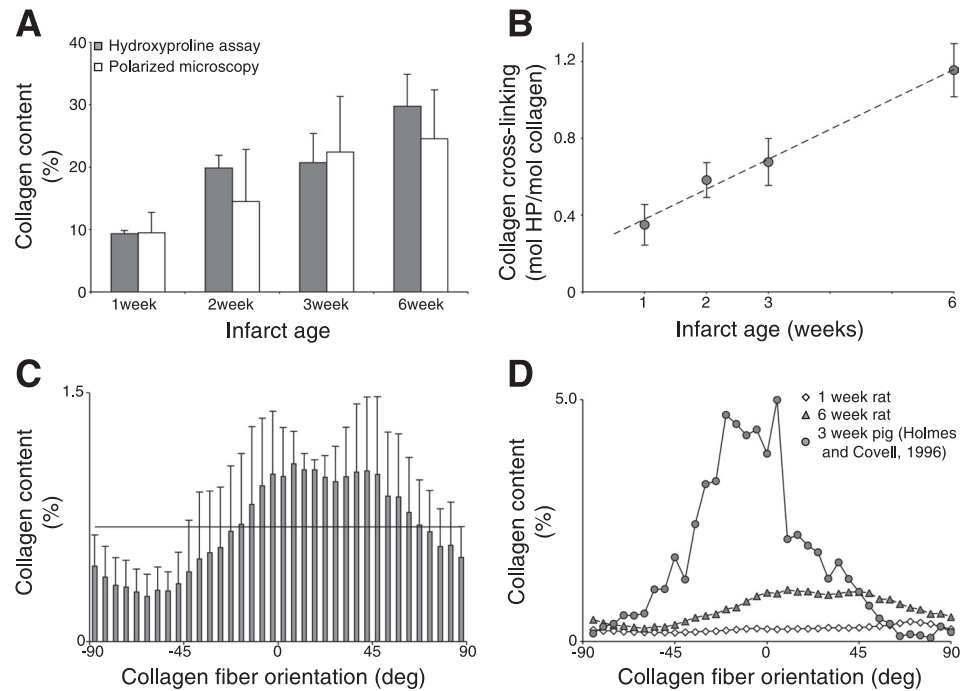
The aliquots for the HP assay (mixed in acetic acid 0.5 ml, cellulose slurry 0.5 ml, *n*-butanol 2 ml) were transferred onto a cellulose column. HP was separated from the other amino acids and impurities by several washes with organic acid-alcohol mobile phase and eluted from the cellulose column with water. HP cross-links were quantified by high-pressure liquid chromatography. The average results from the triplets of each sample were reported as moles of HP per mole of collagen (measured in OH-pro assay above), assuming that the molecular weight of collagen is 300,000.

**Statistical analysis.**  $P < 0.05$  was taken to indicate statistical significance for all tests. Changes in functional and regional strain data between control and acute ischemia were assessed with paired *t*-tests, whereas changes from acute ischemia through the time course of healing were assessed with one-way ANOVA followed by Dunnett multiple comparisons post hoc tests against the acute ischemia group. One-way ANOVA without post hoc tests was used to test whether measured structural and mechanical variables changed significantly with time (Instat 3.0, GraphPad Software, San Diego, CA). Multiple linear regression was used to examine the dependence of functional measures on infarct size, scar collagen content, scar stiffness, and chamber dilation. Collagen alignment data were analyzed by using circular statistics: angles were represented as unit vectors and the vector components were averaged to yield representative mean vectors (1). Alignment was considered statistically significant if the dot products of a group of vectors with their mean vector were statistically different from 0 by a one-sample *t*-test.

## RESULTS

**Scar structure and biochemistry.** Collagen content of the healing scars increased with time (Fig. 2A; ANOVA  $P < 0.05$  for polarized microscopy data,  $P < 0.001$  for hydroxyproline data), with remarkably good agreement between biochemical and polarized microscopy methods. The rise of collagen cross-link concentration with time was nearly linear (Fig. 2B; linear

Fig. 2. Infarct scar composition and structure. *A*: collagen content increased over the time course of healing, with good agreement between biochemical assays and polarized light microscopy. *B*: collagen cross-link concentration increased nearly linearly with time. *C*: mean histograms of collagen orientation showed the greatest deviation from random (horizontal line) at 6 wk but were not significantly different from random at any time point. *D*: collagen histograms scaled by collagen area fraction and plotted as line plots show the dramatic differences in collagen content and alignment between the rat scars studied here and 3-wk-old pig infarct scars studied previously (9).



regression  $r^2 = 0.90$ ,  $P < 0.0001$ ). Infarct scars were structurally isotropic: although the mean histogram appeared to develop a modest peak at 6 wk (Fig. 2C), alignment was not statistically significant at any time point. The structural isotropy throughout healing contrasted sharply with our previous measurements in healing pig infarcts (Fig. 2D).

**Scar mechanics.** Scars were roughly square and relatively thin, with typical dimensions of 1 cm in the circumferential and longitudinal directions and 1–2 mm in the radial direction. Because healing scars were structurally isotropic, we utilized an isotropic constitutive model to fit biaxial stress-strain data. As outlined under METHODS and demonstrated in Fig. 1, plots of  $dW/dI_C$ , the first derivative of the strain energy function with respect to the first invariant of the right Cauchy-Green deformation tensor, suggested a quadratic function of  $I_C$  alone (Eq. 5) as a form for the strain energy function. This model fit biaxial test data well ( $r^2 > 0.80$ ) in all but 3 samples (Fig. 1D). The three scars with lower  $r^2$  had below-average levels of collagen alignment, suggesting that scar anisotropy did not explain the poorer fit of the isotropic model in these cases. The stiffness of the healing scars increased with time (Fig. 3A; ANOVA  $P < 0.05$  for coefficient  $c_1$ ) and collagen content explained nearly half the variation in scar mechanics (Fig. 3B;  $r^2 = 0.42$ ,  $P < 0.001$  for coefficient  $c_1$  vs. collagen content squared).

**LV function.** Open-chest, anesthetized animals showed dilation (increased EDV, ESV, and volume intercept  $V_0$ ), elevated end-diastolic pressure, and reduced systolic function (reduced CO and EF) 15 min after coronary ligation (Table 1). Systolic epicardial strains in the infarct region were negative prior to infarction, indicating normal systolic contraction, and positive during acute ischemia, indicating systolic stretching. At subsequent times during healing, few of these functional indexes changed from their values at acute ischemia. Only HR, LV/BW ratio, and RV/BW ratio increased significantly at later times (Table 1).

Infarction primarily affected the  $V_0$  of the ESPVR rather than its slope ( $E_{max}$ , Fig. 4).  $E_{max}$  did not change significantly during acute ischemia or subsequent healing and displayed no clear relationship with infarct size, collagen content, or global chamber

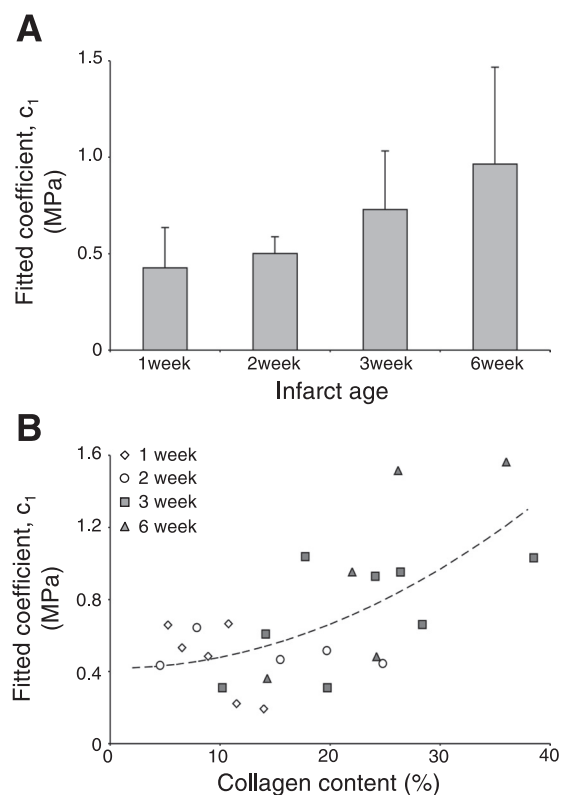


Fig. 3. Infarct scar mechanics. *A*: infarct scar stiffness increased over the time course of healing. *B*: across all time points, the fitted coefficient  $c_1$  correlated significantly with collagen content ( $r^2 = 0.42$  vs. square of collagen content).

Table 1. Hemodynamics, regional deformation, and left ventricular remodeling following infarction in the rat

	Control	Acute	1 wk	2 wk	3 wk	6 wk
EDV, ml	0.48±0.16	0.63±0.20*	0.51±0.10	0.51±0.29	0.65±0.22	0.54±0.25
EDP, cmH <sub>2</sub> O	7±1	12±4*	13±7	7±2	14±7	10±4
ED SA/LA	0.67±0.04	0.65±0.05	0.60±0.06	0.57±0.10	0.63±0.05	0.59±0.05
ESV, ml	0.24±0.12	0.48±0.15*	0.40±0.11	0.38±0.24	0.49±0.22	0.39±0.22
ESP, cmH <sub>2</sub> O	115±21	113±24	110±18	115±12	121±13	123±15
E <sub>max</sub> , cmH <sub>2</sub> O/ml	675±385	497±256	784±268	702±506	576±98	651±241
V <sub>0</sub> , ml	0.04±0.11	0.21±0.13*	0.24±0.12	0.13±0.11	0.27±0.23	0.19±0.22
HR, bpm	287±40	293±40*	359±36†	402±21†	347±26†	388±16†
CO, ml/min	70±19	44±19*	42±16	51±23	53±10	57±26
EF, %	52±11	24±5*	24±12	27±11	26±11	30±16
E <sub>CC</sub>	-0.07±0.04	0.03±0.01*	0.04±0.03	0.04±0.01	0.03±0.02	0.02±0.03
E <sub>LL</sub>	-0.05±0.03	0.05±0.04*	0.05±0.03	0.04±0.02	0.03±0.03	0.04±0.08
LV/BW, mg/g		2.15±0.13	2.45±0.20	2.89±0.31†	2.56±0.24†	2.65±0.18†
RV/BW, mg/g		0.56±0.05	0.64±0.06	0.66±0.12	0.72±0.06†	0.72±0.08†

Values are means ± SD. EDV and EDP, end-diastolic volume and pressure, respectively; ED SA/LA, end-diastolic short-axis/long-axis ratio (index of shape); ESV and ESP, end-systolic volume and pressure, respectively; E<sub>max</sub> and V<sub>0</sub>, slope and intercept, respectively, of end-systolic pressure-volume relationship; HR, heart rate; CO, cardiac output; EF, ejection fraction; E<sub>CC</sub> and E<sub>LL</sub>, circumferential and longitudinal strain, respectively, from end diastole to end systole; LV/BW and RV/BW, ratios of left ventricular and right ventricular weight, respectively, to body weight. \*P < 0.05 vs. control by paired t-test; †P < 0.05 vs. acute by ANOVA and Dunnett's multiple comparisons post hoc.

dilation. By contrast, V<sub>0</sub> increased during acute ischemia, remained elevated during healing, and correlated with a combination of infarct size, collagen content, and global dilation of the LV chamber (r<sup>2</sup> = 0.84, P < 0.0001). The multiple regression equation for V<sub>0</sub> predicted a rightward shift of the ESPVR (depressed function) with increased infarct size or chamber dilation and a leftward shift with increased collagen content (Fig. 4B): V<sub>0</sub> = 254 + 6.38 × [infarct size] - 7.29 × [collagen content] + 0.521 × [V<sub>10</sub>]. Overall, infarct size was the dominant factor in determining systolic function: infarct size alone explained more than half the variation in V<sub>0</sub> (Fig. 4C; r<sup>2</sup> = 0.52, P < 0.001) and a small but statistically significant fraction of infarct-related decreases in EF (Fig. 4D; r<sup>2</sup> = 0.27, P < 0.05).

DISCUSSION

We studied the evolution of scar structure and mechanics during healing of large anterior myocardial infarcts in rats. The key findings were that rat infarcts developed structurally and mechanically isotropic scars, that infarct stiffness appeared to be determined largely by collagen content, and that healing infarcts influenced systolic LV function through a rightward shift of the ESPVR that depended on infarct size, infarct collagen content, and LV dilation.

Structural and mechanical isotropy in healing rat infarcts. The isotropic structure of healing rat infarcts was particularly surprising in light of studies in other animals. Quantitative

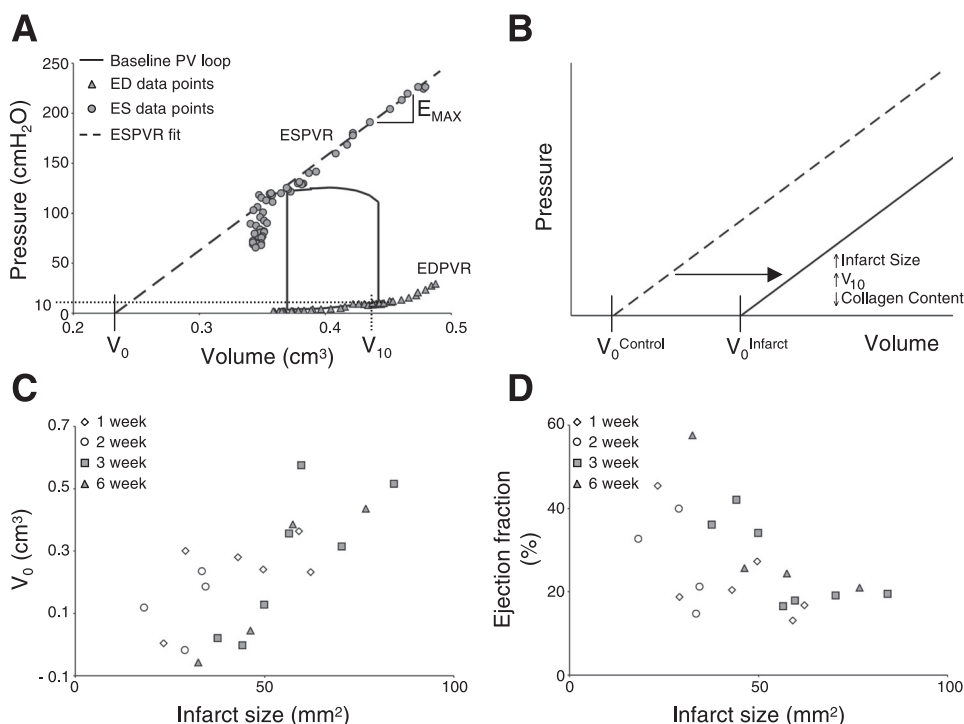


Fig. 4. Determinants of left ventricular (LV) function. A: representative hemodynamic data (MI141, 1-wk group), showing a fit to the linear region of the end-systolic (ES) pressure-volume relationship (ESPVR) and indexes used to evaluate LV function. Schematic pressure-volume (PV) loop indicates the baseline state; higher and lower pressures were obtained by brief occlusion of the aorta and inferior vena cava, respectively. EDPVR, end-diastolic (ED) pressure-volume relationship; E<sub>max</sub>, slope of the ESPVR. B: the main impact of the infarct on systolic function was a parallel shift of ESPVR, reflected in an increased volume intercept (V<sub>0</sub>). C: infarct size alone explained more than half the variation in V<sub>0</sub> (r<sup>2</sup> = 0.52, P < 0.001). D: ejection fraction decreased with infarct size (r<sup>2</sup> = 0.27, P < 0.05).

structural analysis of healing pig (9) and dog (21) scars using polarized light microscopy revealed a high degree of collagen fiber alignment, with mean orientation in the circumferential direction. By contrast, in this study we found no significant collagen alignment at any time point studied. At 3 wk, the length of the vectors representing the orientation of individual rat scar samples ranged from 0.19 to 0.45 (0 = random, 1 = perfectly aligned), and vector orientations ranged from  $-17$  to  $90^\circ$  ( $0^\circ$  = circumferential). Identical calculations with data from Holmes et al. (10) revealed 3-wk pig scars to be both more aligned (vector lengths ranging from 0.48 to 0.71) and more consistently oriented (orientations ranging from  $-21$  to  $-4^\circ$ ). In addition, the average collagen area fraction of  $0.22 \pm 0.09$  we found in 3-wk rat scars in this study was less than half the value of  $0.59 \pm 13$  we computed from the data of Holmes et al., who used slightly thicker sections (10  $\mu\text{m}$ ) but otherwise similar polarized light methods.

We previously suggested that infarct anisotropy may have important advantages in preserving systolic function during postinfarction healing (10) and proposed one mechanism by which this anisotropy might arise (24). Now, the dramatic differences in structural anisotropy between the rat infarcts we studied here and the pig infarcts we studied previously provide a new window on this problem. The rat infarcts were large, roughly circular, and located on the anterior wall near the apex, whereas the pig infarcts were relatively small, long and thin, and located on the lateral wall near the equator. Differences in infarct size and shape could conceivably influence inflammatory cell and fibroblast migration from the infarct margins or the distribution of cytokines and other soluble factors within the infarct, thereby altering collagen deposition. Infarct size, shape, and location could also influence collagen deposition by altering regional mechanics, and our data provide some support for this idea. Healing rat infarcts stretched equally in the circumferential and longitudinal directions at each time point studied (Table 1), whereas the pig infarcts we studied previously stretched only in the circumferential direction (10). We hypothesize that the local pattern of stretching determines collagen alignment in the healing scar.

Consistent with the observed structural isotropy, we found healing rat infarcts to be mechanically isotropic. Other groups have studied infarct mechanics in different animal models (3, 6, 8, 14). Most of them studied deformation of the infarcted region during LV inflation or performed uniaxial testing on strips of excised infarcts. Both of these methods have important limitations: geometric complexity of the LV and the attachment of the infarcted region to adjacent healthy myocardium make the task of estimating stresses that act on the infarct in the intact ventricle extremely challenging, whereas uniaxial tests on strips of infarct scars are of limited value in investigating material anisotropy. There is a single previous study that reported planar biaxial testing of infarct scars: Gupta et al. (6) investigated the evolution of sheep infarct mechanical properties and found sheep scars to be mechanically anisotropic, with a degree and direction of anisotropy that changed over time. Because collagen fiber orientation was not measured in that study, the structural basis for the mechanical anisotropy was unclear. However, it seems clear that, like structural anisotropy, mechanical anisotropy can vary among different animal models.

*Collagen content, cross-linking, and scar mechanics.* The most surprising finding of Gupta et al.'s study (6) was that,

after an initial rise, infarct stiffness decreased from 2 to 6 wk, whereas collagen content continued to increase. This decoupling of infarct stiffness from collagen content prompted some to hypothesize that collagen cross-link density determines infarct mechanics after the early stages of healing (8). In the present study, we found that infarct stiffness increased steadily with time and correlated significantly with collagen content. Between 3 and 6 wk of healing, scar stiffness and collagen content increased only moderately, whereas collagen cross-link density nearly doubled, indicating that collagen cross-linking had a modest effect on infarct mechanics compared with collagen content in this infarct model. Overall, our results are consistent with several early uniaxial studies (3, 14, 16) and inconsistent only with Gupta's study. Given our new findings and numerous consistent studies in several animal models, we conclude that collagen content and structure are likely the primary determinants of infarct mechanics through the first 6 wk of healing.

We used two methods in the structural analysis of infarct scars: polarized microscopy and biochemistry. Although each method provided additional information (collagen fiber alignment and cross-link density, respectively); the level of agreement between the two methods on collagen content data was an important result in itself. In establishing the method of circularly polarized microscopy, Whittaker et al. (22) validated the technique against data obtained by manual point counting. Our report of the direct agreement between circular polarized microscopy and the well-established hydroxyproline assay method serves to further validate circular polarized microscopy for analysis of collagen content as well as orientation.

*Infarct mechanics and LV function.* We investigated the effect of infarct size, infarct mechanics, and overall chamber dilation on LV function. Early finite-element modeling studies by Bogen et al. (2) suggested that changes in infarct mechanics at different stages of healing should primarily affect LV function by altering  $E_{\text{max}}$ , the slope of the ESPVR. Sunagawa et al. (20) studied acute regional ischemia rather than healing infarcts, but their experimental evidence and a simple compartmental model showed that the main effect of ischemia on systolic function was a rightward shift of ESPVR, reflected in an increase in the volume intercept  $V_0$  rather than a change in  $E_{\text{max}}$ . Our measurements at different stages of infarct healing confirm and extend Sunagawa's analysis of acute ischemia: we observed an increase in  $V_0$  that depended on infarct size, collagen content, and LV dilation, whereas  $E_{\text{max}}$  did not change significantly with time or correlate with any of these factors.

Sunagawa's compartmental model predicts the slope and intercept of the ESPVR of an ischemic or infarcted LV by using weighted averages of the high-pressure portion of the control ESPVR and EDPVR, treating the ischemic region as passive myocardium stretched to systolic pressures. In Sunagawa's experiments, the slopes of the high-pressure portions of the control ESPVR and EDPVR were similar, so his model predicted little change in slope, in agreement with his data. In examining Bogen's model closely, we found that he used ESPVR and EDPVR curves that differed by severalfold in slope at systolic pressures; in this case, Sunagawa's model would also predict a significant decrease in  $E_{\text{max}}$  with increasing ischemic region size. The choice of control ESPVR and EDPVR, not the modeling approach, explains the disagreement between these two published models.

Although our results show that many factors considered play some role in determining ventricular function, infarct size clearly dominated. This finding is consistent with previous studies in the rat coronary ligation model, which showed that functional depression at 3 wk (18) and LV remodeling beyond 1 wk (17) both depended heavily on infarct size. To isolate and further study the effect of infarct mechanical properties on LV function and remodeling, it would be necessary to use an experimental model in which infarct size can be controlled much more precisely.

**Limitations and sources of error.** The most important potential sources of error in this study related to the mechanical testing of these very small samples. In general, we prefer several independent attachment points per side for biaxial testing, but in this study we were limited to two per side by the small size of the scar samples. Estimating the unloaded area (sample thickness and effective side length) for stress computation was also challenging in these very small samples. We attempted to limit the impact of these error sources by conducting finite element simulations to confirm that stresses were uniform in the central region with just two attachment points per side and that our definition of effective side length provided reasonable stress estimates. Remaining errors may have affected the absolute value of the computed stresses but should not have affected relative stress magnitudes in different directions or the key finding that the scar samples were mechanically isotropic. Another limitation of these studies is that functional data were obtained in open-chest, anesthetized rats. We would therefore expect these data to underestimate ventricular function but would expect that overall trends with infarct size, collagen content, etc. remain valid.

**Conclusions.** We studied the evolution of scar structure and mechanics during healing of large anterior myocardial infarcts in rats. As expected, healing infarcts influenced systolic LV function through a rightward shift of the ESPVR that depended on infarct size, infarct collagen content, and LV dilation. In sharp contrast to previous reports in large animal models, however, rat infarcts developed structurally and mechanically isotropic scars in which infarct stiffness appeared to be determined largely by collagen content. On the basis of the regional strain patterns we observed in healing rat infarcts in this study and in healing pig infarcts in previous studies, we hypothesize that the local pattern of stretching determines collagen alignment in healing myocardial infarct scars.

## APPENDIX

### Computing Stresses During Biaxial Testing With In-Plane Shear

During planar biaxial testing, it is common to assume a state of plane stress, with all stress components involving the third direction (perpendicular to the sample) equal to zero; out-of-plane deformations are also assumed to be zero, except for changes in the sample thickness that arise due to the Poisson effect. The nonzero components of the Cauchy stress tensor  $\mathbf{t}$  and deformation gradient tensor  $\mathbf{F}$  can be written (11)

$$[\mathbf{t}] = \begin{bmatrix} t_{11} & t_{12} & 0 \\ t_{21} & t_{22} & 0 \\ 0 & 0 & 0 \end{bmatrix} \quad \text{and} \quad (A1)$$

$$[\mathbf{F}] = \begin{bmatrix} \lambda_1 & \kappa_1 & 0 \\ \kappa_2 & \lambda_2 & 0 \\ 0 & 0 & \lambda_3 \end{bmatrix}. \quad (A2)$$

The in-plane components of  $\mathbf{F}$  are easily measured, whereas  $F_{33}$  is not; for biological materials, it is common to assume incompressibility and compute  $\lambda_3$  as

$$F_{33} = \lambda_3 = 1/(F_{11}F_{22} - F_{12}F_{21}). \quad (A3)$$

The components of the Cauchy stress tensor  $\mathbf{t}$  can be calculated using measured forces and cross-sectional areas and the definition of the stress tensor (11):

$$\mathbf{f} = \mathbf{n} \cdot \mathbf{t}a, \quad (A4)$$

where  $\mathbf{f}$  is the force vector acting in a chosen direction,  $\mathbf{n}$  is the unit normal specifying that direction, and  $a$  is the current cross-sectional area perpendicular to the normal, on which the force is acting. It is usually much easier to measure cross-sectional area in the initial, undeformed configuration than to track it during biaxial testing. Therefore, many investigators employ the first Piola-Kirchhoff stress tensor  $\mathbf{P}$ , which is defined in terms of current force and original, undeformed cross-sectional area  $A$ :

$$\mathbf{f} = \mathbf{N} \cdot \mathbf{P} A. \quad (A5)$$

Prior planar biaxial tests of soft tissues (19, 23) assumed that shear deformations ( $\kappa_1$  and  $\kappa_2$  in Eq. A2) are negligible. In this case, the applied forces maintain the same orientation with respect to the sample throughout the test ( $\mathbf{n} = \mathbf{N} = \mathbf{e}_1$  or  $\mathbf{e}_2$ ) and the only nonzero stress components are

$$t_{11} = f_1/a_1, \quad t_{22} = f_2/a_2, \quad (A6)$$

$$P_{11} = f_1/A_1, \quad P_{22} = f_2/A_2, \quad (A7)$$

where  $f_1$  and  $f_2$  indicate forces along the  $x_1$  and  $x_2$  test axes,  $a_1$  and  $a_2$  the current cross-sectional areas on which those forces are acting, and  $A_1$  and  $A_2$  the undeformed cross-sectional areas. Biological materials with a preferred fiber direction will shear during biaxial testing unless the fibers are aligned with one test axis or the samples are rigidly clamped at the edges. When shearing is not negligible, both the direction of the applied forces relative to the sample and the relevant cross-sectional areas change throughout the test; the changing stresses, unit normals, and cross-sectional areas are related by

$$\mathbf{t} = (1/J)\mathbf{F} \cdot \mathbf{P}, \quad \text{and} \quad (A8)$$

$$\mathbf{N} dA = \mathbf{n} \cdot \mathbf{F}(da/J), \quad (A9)$$

where  $J$  is the determinant of  $\mathbf{F}$ .

Our biaxial testing device uses multiple attachment points and allows redistribution of tension among sutures on each side of the sample; it applies force along the same axes throughout the test ( $\mathbf{n} = \mathbf{e}_1$  or  $\mathbf{e}_2$ ) but allows samples to shear. Along the first test axis ( $\mathbf{n} = \mathbf{e}_1$ ), the current force  $f_1$  is related to the Cauchy stress components and cross-sectional area  $a_1$  by

$$f_1 \mathbf{e}_1 = [1 \quad 0 \quad 0] \cdot \begin{bmatrix} t_{11} & t_{12} & 0 \\ t_{21} & t_{22} & 0 \\ 0 & 0 & 0 \end{bmatrix} a_1 = a_1 [t_{11} \quad t_{12} \quad 0] \quad (A10)$$

The fact that the device applies force only along the  $x_1$  axis requires that  $t_{12} = 0$ . Using a similar logic for the second test direction, we find that the only nonzero components of the Cauchy stress are those given by Eq. A6. In the presence of shear, however, Eq. A7 no longer holds. Substituting the expressions A6 into Eq. A8 and solving for  $\mathbf{P}$  gives the nonzero components of the first Piola-Kirchhoff stress tensor:

$$\begin{aligned} P_{11} &= \lambda_2 \lambda_3 t_{11}, \\ P_{12} &= -\kappa_1 \lambda_3 t_{22} = (-\kappa_1/\lambda_1)P_{22}, \\ P_{21} &= -\kappa_2 \lambda_3 t_{11} = (-\kappa_2/\lambda_2)P_{11}, \quad \text{and} \\ P_{22} &= \lambda_1 \lambda_3 t_{22}. \end{aligned} \quad (A11)$$

Equations A6 and A11 assume that the appropriate deformed cross-sectional areas  $a_1$  and  $a_2$  are known, but usually they are not. Employing Eq. A9 for the first test axis,

$$\mathbf{N}_1 \mathbf{A}_1 = \frac{1}{J} \mathbf{n}_1 a_1 \cdot \mathbf{F} = \frac{a_1}{J} \begin{bmatrix} 1 & 0 & 0 \end{bmatrix} \cdot \begin{bmatrix} \lambda_1 & \kappa_1 & 0 \\ \kappa_2 & \lambda_2 & 0 \\ 0 & 0 & \lambda_3 \end{bmatrix} \quad (A12)$$

$$= \frac{a_1}{J} [\lambda_1 \quad \kappa_1 \quad 0],$$

and it follows directly that

$$\mathbf{N}_1 = \frac{1}{\sqrt{\lambda_1^2 + \kappa_1^2}} [\lambda_1 \quad \kappa_1 \quad 0], \text{ and} \quad (A13)$$

$$A_1 = \frac{a_1}{J} \sqrt{\lambda_1^2 + \kappa_1^2}. \quad (A14)$$

Combining equations A6 and A14 and noting that  $J = 1$  for incompressible materials provides an experimentally convenient expression for the Cauchy stress component  $t_{11}$ ; a similar calculation for the second test direction completes the derivation of Eq. 2 in the main text:

$$t_{11} = \frac{f_1}{a_1} = \frac{f_1}{A_1} \sqrt{\lambda_1^2 + \kappa_1^2}, \quad t_{22} = \frac{f_2}{a_2} = \frac{f_2}{A_2} \sqrt{\lambda_2^2 + \kappa_2^2}, \quad (A15)$$

$$t_{12} = t_{21} = t_{13} = t_{31} = t_{32} = t_{23} = t_{33} = 0.$$

As a consistency check, inserting expressions for  $P_{ij}$  (Eq. A11),  $\mathbf{N}_1$  (Eq. A13), and  $A_1$  (Eq. A14) into Eq. A5 yields:

$$\mathbf{N}_1 \cdot \mathbf{P} \mathbf{A}_1 = \frac{1}{\sqrt{\lambda_1^2 + \kappa_1^2}} [\lambda_1 \quad \kappa_1 \quad 0]$$

$$\times \begin{bmatrix} \lambda_2 \lambda_3 t_{11} & -\kappa_1 \lambda_3 t_{22} & 0 \\ -\kappa_2 \lambda_3 t_{11} & \lambda_1 \lambda_3 t_{22} & 0 \\ 0 & 0 & 0 \end{bmatrix} \frac{a_1}{J} \sqrt{\lambda_1^2 + \kappa_1^2}$$

$$= \frac{a_1}{J} [(\lambda_1 \lambda_2 - \kappa_1 \kappa_2) \lambda_3 t_{11} \quad (-\kappa_1 \lambda_1 + \kappa_1 \lambda_1) \lambda_3 t_{22} \quad 0]$$

$$= \frac{a_1}{J} [J t_{11} \quad 0 \quad 0]$$

$$= a_1 [t_{11} \quad 0 \quad 0]$$

$$= \mathbf{n}_1 \cdot \mathbf{t} a_1$$

#### ACKNOWLEDGMENTS

The authors acknowledge the assistance of Dr. David Paik in performing the biochemical analyses of collagen content and cross-linking.

#### GRANTS

This work was funded by a grant from the National Institutes of Health (HL-075639).

#### DISCLOSURES

No conflicts of interest are declared by the author(s).

#### REFERENCES

1. Batschelet E. *Circular Statistics in Biology*. London: Academic, 1981.

2. Bogen DK, Rabinowitz SA, Needleman A, McMahon TA, Abelmann WH. An analysis of the mechanical disadvantage of myocardial infarction in the canine left ventricle. *Circ Res* 47: 728–741, 1980.
3. Connelly CM, Vogel WM, Wiegner AW, Osmers EL, Bing OH, Kloner RA, Dunn-Lanchantin DM, Franzblau C, Apstein CS. Effects of reperfusion after coronary artery occlusion on post-infarction scar tissue. *Circ Res* 57: 562–577, 1985.
4. Fishbein MC, Maclean D, Maroko PR. Experimental myocardial infarction in the rat: qualitative and quantitative changes during pathologic evolution. *Am J Pathol* 90: 57–70, 1978.
5. Frohlich MW. Birefringent objects visualized by circular polarization microscopy. *Stain Technol* 61: 139–143, 1986.
6. Gupta KB, Ratcliffe MB, Fallert MA, Edmunds LH Jr, Bogen DK. Changes in passive mechanical stiffness of myocardial tissue with aneurysm formation. *Circulation* 89: 2315–2326, 1994.
7. Holmes JW. Candidate mechanical stimuli for hypertrophy during volume overload. *J Appl Physiol* 97: 1453–1460, 2004.
8. Holmes JW, Borg TK, Covell JW. Structure and mechanics of healing myocardial infarcts. *Annu Rev Biomed Eng* 7: 223–253, 2005.
9. Holmes JW, Covell JW. Collagen fiber orientation in myocardial scar tissue. *Cardiovasc Pathobiol* 1: 15–22, 1996.
10. Holmes JW, Nunez JA, Covell JW. Functional implications of myocardial scar structure. *Am J Physiol Heart Circ Physiol* 272: H2123–H2130, 1997.
11. Humphrey JD. *Cardiovascular Solid Mechanics: Cells, Tissues, and Organs*. New York: Springer-Verlag, 2002.
12. Humphrey JD, Strumpf RK, Yin FC. Determination of a constitutive relation for passive myocardium: I. A new functional form. *J Biomech Eng* 112: 333–339, 1990.
13. Karlton WJ, Covell JW, McCulloch AD, Hunter JJ, Omens JH. Automated measurement of myofiber disarray in transgenic mice with ventricular expression of ras. *Anat Rec* 252: 612–625, 1998.
14. Lerman RH, Apstein CS, Kagan HM, Osmers EL, Chichester CO, Vogel WM, Connelly CM, Steffee WP. Myocardial healing and repair after experimental infarction in the rabbit. *Circ Res* 53: 378–388, 1983.
15. McCormick RJ, Musch TI, Bergman BC, Thomas DP. Regional differences in LV collagen accumulation and mature cross-linking after myocardial infarction in rats. *Am J Physiol Heart Circ Physiol* 266: H354–H359, 1994.
16. Parnley WW, Chuck L, Kivowitz C, Matloff JM, Swan HJ. In vitro length-tension relations of human ventricular aneurysms. Relation of stiffness to mechanical disadvantage. *Am J Cardiol* 32: 889–894, 1973.
17. Pfeffer JM, Pfeffer MA, Fletcher PJ, Braunwald E. Progressive ventricular remodeling in rat with myocardial infarction. *Am J Physiol Heart Circ Physiol* 260: H1406–H1414, 1991.
18. Pfeffer MA, Pfeffer JM, Fishbein MC, Fletcher PJ, Spadaro J, Kloner RA, Braunwald E. Myocardial infarct size and ventricular function in rats. *Circ Res* 44: 503–512, 1979.
19. Sacks MS, Chuong CJ. Orthotropic mechanical properties of chemically treated bovine pericardium. *Ann Biomed Eng* 26: 892–902, 1998.
20. Sunagawa K, Maughan WL, Sagawa K. Effect of regional ischemia on the left ventricular end-systolic pressure-volume relationship of isolated canine hearts. *Circ Res* 52: 170–178, 1983.
21. Whittaker P, Boughner DR, Kloner RA. Analysis of healing after myocardial infarction using polarized light microscopy. *Am J Pathol* 134: 879–893, 1989.
22. Whittaker P, Kloner RA, Boughner DR, Pickering JG. Quantitative assessment of myocardial collagen with picosirius red staining and circularly polarized light. *Basic Res Cardiol* 89: 397–410, 1994.
23. Yin FC, Strumpf RK, Chew PH, Zeger SL. Quantification of the mechanical properties of noncontracting canine myocardium under simultaneous biaxial loading. *J Biomech* 20: 577–589, 1987.
24. Zimmerman SD, Karlton WJ, Holmes JW, Omens JH, Covell JW. Structural and mechanical factors influencing infarct scar collagen organization. *Am J Physiol Heart Circ Physiol* 278: H194–H200, 2000.